Coseismic displacement field and slip distribution of the 2005 Kashmir earthquake from SAR amplitude image correlation and differential interferometry

Yajing Yan, Virginie Pinel, Emmanuel Trouvé, Erwan Pathier, Jonathan Perrin, Pascale Bascou, François Jouanne

Geophysical Journal International

Geophys. J. Int. (2013) **193,** 29–46 doi: 10.1093/gji/ggs102

Coseismic displacement field and slip distribution of the 2005 Kashmir earthquake from SAR amplitude image correlation and differential interferometry

Y. Yan,[1,2] V. Pinel,[2] E. Trouvé,[1] E. Pathier,[2] J. Perrin,[2] P. Bascou[2] and F. Jouanne[2]

[1] *Laboratoire d'Informatique, Systèmes, Traitement de l'Information et de la Connaissance, Université de Savoie - Polytech Annecy-Chambéry,* BP 80439, F-74944, *Annecy-le-Vieux Cedex, France. E-mail: yajing.yan@ulg.ac.be*

[2] *Institut des Sciences de la Terre, IRD* R219, *CNRS, Université de Savoie - Campus Scientifique* - 73376 - *Le Bourget du Lac Cedex, France; and Université de Grenoble* 1, BP53 - 38041- *Grenoble, France*

Accepted 2012 December 4. Received 2012 December 4; in original form 2012 April 28

SUMMARY

The coseismic surface displacement field and slip distribution at depth due to the Kashmir earthquake ($M_w = 7.6$, 2005) have been analysed by different authors using subpixel correlation of synthetic aperture radar (SAR) images and optical images, teleseismic analysis, GPS measurements, as well as *in situ* field measurements. In this paper, first, we use 23 sets of measurement from subpixel correlation of SAR images and differential interferometry to retrieve the 3-D coseismic surface displacement field. The obtained horizontal and vertical components along the fault trace are then compared, respectively, to equivalent measurements obtained from subpixel correlation of two optical ASTER images and *in situ* field measurements. Second, the coseismic fault geometry parameters and slip distribution at depth are estimated. In addition to the one segment slip model as reported in previous work, a two segments slip model that better fits the surface fault break is proposed. The improvement of the two segments slip model in interpreting the measured displacement field is highlighted through comparison of residuals of both slip models. Taking advantage of differential interferometry measurements that provide precise and continuous information in the far field of the fault, firstly, a wedge thrust according to Bendick *et al.* to the Northwest of the main rupture built on our two segments model is tested. According to the obtained results, the residual of the two segments main rupture plus wedge thrust model is slightly smaller than the residual of the two segments model to the Northwest of the Balakot–Bagh fault. Secondly, we test the sensitivity of our slip model to the presence of slip along a décollement as evidenced by Jouanne *et al.* through post-seismic analysis. The results indicate that the estimations of the coseismic displacement field and slip distribution in this paper are not significantly biased by such post-seismic displacement and that most coseismic displacement is located on a $\sim 40^\circ$ NE-dipping fault, as previously reported.

Key words: Image processing; Earthquake ground motions; Dynamics and mechanics of faulting.

1 INTRODUCTION

An earthquake of $M_w = 7.6$ struck the Northern Pakistan (Kashmir region) in an out-of-sequence position, 100 km North of the Main Frontal Thrust, on 8 October 2005, causing 87 000 deaths. This earthquake occurred along the Himalayas, a tectonic boundary formed by the collision of the Indian and Eurasian Plates and characterized by high seismic activity as illustrated by the occurrence of earthquakes of $M_w \backsimeq 8$ in the historical seismicity (Bilham *et al.* 1998; Kumar *et al.* 2001; Lavé *et al.* 2005). During this earthquake, a NE-dipping thrust fault, from Bagh to Balakot via the Jhelum river valley and the city of Muzaffarabad (Fig. 1), was activated (Avouac *et al.* 2006; Pathier *et al.* 2006; Kaneda *et al.* 2008). After the main shock, aftershocks continued daily, with more than 978 aftershocks of $M_w = 4.0$ and above recorded before 27 October 2005.

The coseismic surface displacement field, the fault geometry and the slip distribution on the fault due to this earthquake have been analysed by different authors. In Pathier *et al.* (2006) and Wang *et al.* (2007), the 3-D surface displacement (E, N, Up), the fault geometry and the slip distribution are estimated by subpixel correlation of ENVISAT synthetic aperture radar (SAR) images. Avouac *et al.* (2006) used subpixel correlation of two optical advanced

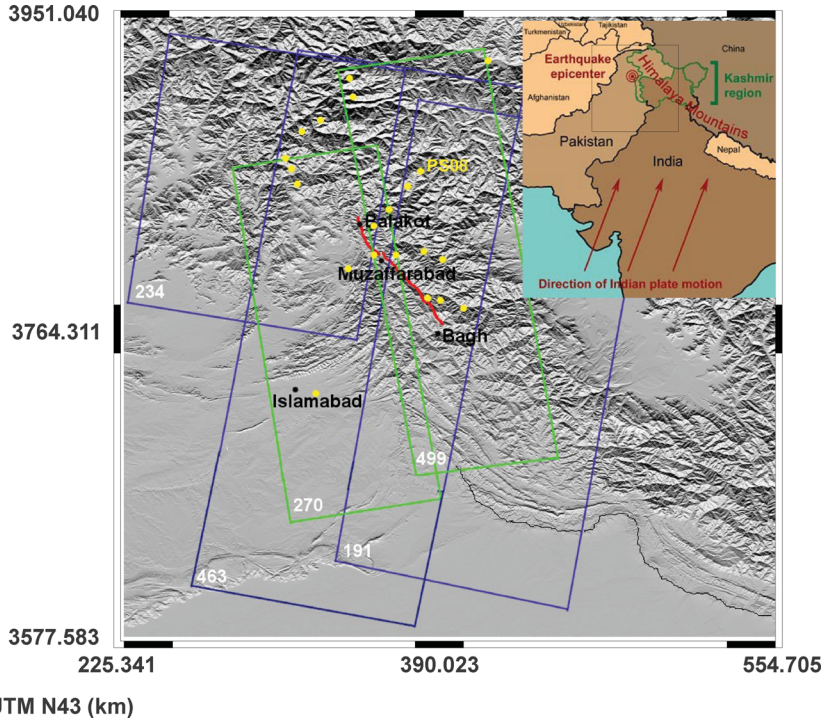

Figure 1. Location of the coseismic data sets (ENVISAT) used in this paper. The Balakot–Bagh thrust activated during the 8 October, 2005 earthquake is drawn in red. This thrust is clearly out-of-sequence as shown by its location, 100 km North of the Main Frontal Thrust (the black line) located at the Southern foothill of the first relief. Track 191, 234, 463 are descending tracks. Tracks 270, 499 are ascending tracks. For tracks 270, 463, 499, there are several scenes corresponding to different frame. Yellow points represent the positions of the GPS measurement dedicated to the post-seismic displacement quantification used in Jouanne *et al.* (2011).

spaceborne thermal emission and reflection radiometer (ASTER) images in order to deduce the horizontal surface displacement (E, N). They combined this information with teleseismic analysis to infer the fault geometry and the slip distribution. In Kaneda *et al.* (2008), *in situ* field measurements are performed to map the surface fault rupture and to measure the vertical surface displacement at the fault. Also, Parsons *et al.* (2006) analysed the static stress change associated with this earthquake by using teleseismic waveforms. According to these analyses, this earthquake corresponds mainly to a thrust fault rupture of about 70 km long, dipping $\sim 30^\circ$ NE, situated between the surface and 15 km depth.

Bendick *et al.* (2007) inferred that this earthquake occurred on a wedge fault with multiples fault planes by combining GPS surface displacement measurements and aftershock locations, including a main rupture between Bagh and Balakot with strike 331° and dip 29°, a NNE-dipping fault plane extending WNW from Balakot and a nearly flat décollement at 5 km depth. However, the data used by Bendick *et al.* (2007) were obtained along the Indus valley, Northwest of the rupture area terminating at Balakot according to the surface observation. The strong aftershocks observed near the Indus valley, Northwest of the rupture area, reflect the activation of the active thrusts with no surface expression that were already activated by the 1974 Pattan earthquake (Jouanne *et al.* 2011). Consequently, the questions arise: is the surface displacement observed by Bendick *et al.* (2007) linked with the strong aftershocks which occurred in this area; and does the main rupture plus wedge thrust model interpret the measured displacement field better than the only main rupture model?

Jouanne *et al.* (2011) analysed the post-seismic displacement based on six GPS campaigns performed in January and August 2006, in March and December 2007, in August 2008 and 2009, between a few hundred meters and several tens of kilometres from the emergence of the thrust (Fig. 1). By comparison to numerical simulations, they propose that post-seismic displacement and aftershock spatial and temporal distribution were probably induced by an afterslip along a décollement North of the ramp affected by the main shock. This mechanism was active at least during the first weeks following the main shock. After this period, afterslip and viscous relaxation with a non-Newtonian viscosity both can explain the recorded post-seismic displacement. The décollement proposed by Jouanne *et al.* (2011) is connected to the ramp and dips 10° North. The displacement along this décollement reached 30.8 cm between November 2005 and August 2006. They conclude that the coseismic surface displacement was induced by the slip on the ramp, while the post-seismic displacement was probably induced by the afterslip along the décollement located NE of the ramp. This conclusion is consistent with the post-seismic behaviour of the Chi-Chi earthquake (Hsu *et al.* 2002; Yu *et al.* 2003; Perfettini and Avouac 2004; Hsu *et al.* 2007) where the afterslip was concentrated on a near-horizontal décollement South and down-dip of the ramp on which the coseismic slip was produced. However, in the case of the main shock of the Kashmir earthquake, the coseismic displacement is essentially constrained by the near field data (except for the teleseismic waveform) or point instantaneous far field data providing poor resolution on potential slip on a deep décollement located between 15 and 30 km in depth, North of the ramp. Consequently, it seems important to estimate how much this conclusion might be biased by the spatial distribution of the data used to retrieve the coseismic displacement field and slip distribution. Another related question is the impact of post-seismic displacement on coseismic

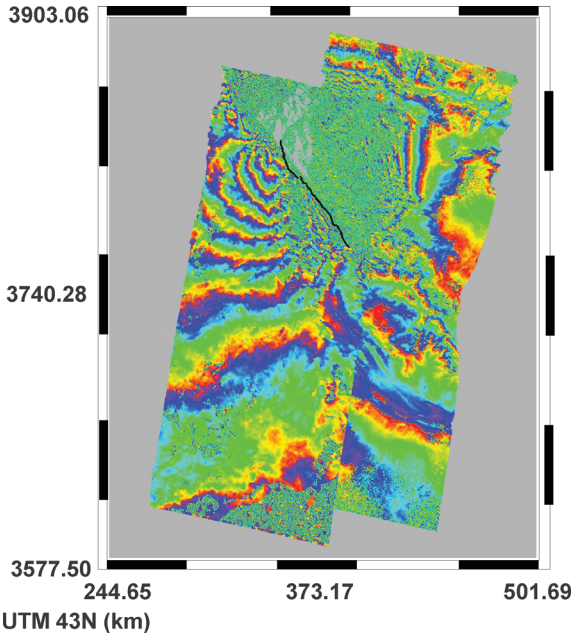

Figure 2. Mosaïc of interferograms. Only two interferograms are displayed (Track 463[1] (2004/11/06–2005/11/26) on the left, Track 191 (2004/10/18–2005/11/07) on the right), because the other three interferograms are superimposed on these two interferograms. The black line represents the surface fault break.

displacement analysis, if the coseismic data include the post-seismic period. Hence, it is necessary to add far field data, such as differential interferometry (D-InSAR) data.

A series of ENVISAT SAR images in both ascending and descending modes, acquired from July 2004 to June 2006, are available to deduce the coseismic fault geometry parameters and slip distribution at depth. The spatial coverage of these data extends from the near field to the far field of the fault, ranging of about 400 km in the NS direction and 250 km in the EW direction, respectively (Fig. 1). Subpixel correlation and D-InSAR are applied to these SAR images in order to extract displacement in range and azimuth directions of each acquisition (hereafter denoted by radar measurements). D-InSAR is applied successfully for the first time to displacement measurement for this earthquake. Since D-InSAR data provide precise displacement information in the far field of the fault (Fig. 2), the use of D-InSAR measurements allows a new contribution to the displacement measurement and fault rupture modelling for this earthquake with respect to previous work.

Firstly, the 3-D surface displacement (E, N, Up) is retrieved by a least squares inversion from radar measurements. Also, subpixel correlation is applied to the same two optical ASTER images as in Avouac *et al.* (2006) in order to estimate the horizontal surface displacement, with two components (E, N). The horizontal displacement and vertical displacement obtained from radar measurements are compared to the horizontal displacement obtained from optical measurements and the vertical displacement obtained from *in situ* field measurements (Kaneda *et al.* 2008), respectively. Then, two slip models with one segment and two segments, respectively, are proposed and the corresponding coseismic fault geometry parameters and slip distribution are estimated using radar measurements. The obtained slip models are further evaluated by residual analysis. Moreover, a wedge thrust inspired from Bendick *et al.* (2007) is tested. Its contribution to interpreting the measured displacement field in and to the NW of the main rupture is discussed. Furthermore, the precise information brought by D-InSAR measurements in the far field of the fault is used to discuss the impact of the post-seismic displacement probably induced by afterslip along a décollement on the retrieved coseismic displacement field and slip distribution, as well as the potential presence of coseismic slip along the décollement level.

2 SAR DATA PROCESSING

Subpixel correlation of SAR image processing is described briefly in this section, since it corresponds to a classical correlation technique provided by ROIPAC (Rosen *et al.* 2004). D-InSAR processing is presented in detail, because a specific phase unwrapping chain, taking prior displacement information into account and using multiscale phase gradient, is developed. Using this processing chain, D-InSAR is applied successfully for the first time to displacement measurement for this earthquake.

2.1 Subpixel image correlation of SAR images

The subpixel image correlation technique has been widely used for the measurement of large amplitude displacements (Michel *et al.* 1999a,b). It consists of a subpixel offset measurement in lines and in columns between the master image and the slave image, which corresponds in SAR images to the displacement in range and azimuth directions, respectively. In general, the accuracy of this technique depends on the image resolution, for ERS and ENVISAT satellite images, it is included between 0.2 and 1.0 m (Pathier *et al.* 2006). Nine pairs of SAR images, in which two pairs are in common with those used by Pathier *et al.* (2006), are correlated using ROIPAC (Rosen *et al.* 2004). A post-processing chain including topographic correction, filtering, thresholding, constant correction, geometric correction, was applied to obtain the final displacement (This post-processing chain is available on line: http://www.efidir.fr). 18 sets of measurement in range and azimuth directions are obtained. We use the pseudo-variance parameter provided by ROIPAC, which quantifies the quality of correlation, as the uncertainty associated with the displacement measurement as in Casu *et al.* (2011).

2.2 Differential interferometry

The application of D-InSAR has not been successful in measuring the displacement due to this earthquake because of the coherence loss and the large gradient of deformation which resulted in aliasing problem. Only a few isolated areas of deformation signal are detected, which made the phase unwrapping extremely difficult. Given this difficulty, we have developed a dedicated processing chain which can take prior displacement information into account (This processing chain is available on line: http://www.efidir.fr.). In our phase unwrapping processing chain, the interferogram fringes are characterized by estimating their phase gradients at different scales (S_0 corresponding to the full resolution SLC image and S_n to the multilooking image after a complex average of n looks in range and $5n$ looks in azimuth). Then these phase gradients are combined in order to reduce noise, as well as to avoid the aliasing problem. Finally, the interferometric phase is unwrapped at scale S_2 from the combined phase gradients using a global least squares method as proposed by Ghiglia & Romero (1994).

2.2.1 *Estimation of multiscale phase gradient*

The estimation of the phase gradient, corresponding to the frequency of a signal, named local frequency in Trouvé *et al.* (1998), can be seen as a problem of spectral analysis on small windows (taking the circularity of the wrapped phase into account, there is no detection of 2π shift at the edge of the fringe). The bi-dimensional phase gradient ($\mathbf{f}_x$, $\mathbf{f}_y$) is estimated by an algorithm based on the multiple signal classification (MUSIC) method (Trouvé *et al.* 1998). For each pixel of the interferogram, besides the estimated phase gradient, an associated confidence parameter indicating the presence of unreliable phase gradient, is provided by this algorithm. The performance of the estimation depends on the size of the estimation window with respect to the fringe width. Typically, with a signal vector of nine pixels (3×3) and an auto-correlation matrix estimated on a window of 9×9 pixels, the estimation is robust for relatively narrow fringes. With the presence of significant noise, larger fringes require a larger estimation window or a reduction of resolution together with low-pass filtering. In practice, in order to respect the local stationarity and to minimize the computation time, we apply the phase gradient estimation at multiscale.

2.2.2 *Fusion of phase gradients*

At the initial scale level (S_1 for example), the estimation of large fringes in the far field of the fault is not always reliable, especially with the presence of significant noise. The transition from high-resolution scale levels (S_1, S_2) to low-resolution scale levels (S_4, S_8, S_{16}) is performed by complex multilooking. This transition greatly reduces the noise, therefore, working at low-resolution scale levels can ensure the quality of phase unwrapping thereafter. However, except for noise reduction, the transition to low-resolution scale level reduces also the fringe width, and this can result in aliasing problems, mostly in the areas close to the fault where the gradient of deformation is very large. Accordingly, in the far field of the fault, we work at low-resolution level scales, while in the near field, we work at a relatively high-resolution scale level depending on the gradient of deformation. Thus, *a priori* displacement information is necessary. For this, we use the 3-D surface displacement field estimated by Pathier *et al.* (2006) by inversion of subpixel image correlation measurements using an homogeneous, elastic, half-space dislocation model (Fig. 3a). For each interferogram, the 3-D surface displacement (E, N, Up) provided by the model is projected into the LOS direction using the corresponding projection vectors. Then we calculate the gradient of deformation, which is used to determine the lowest resolution scale level of phase gradient (Fig. 3b), allowing phase unwrapping without aliasing problem. Finally, multiscale phase gradients are fused into the phase gradient at scale S_2.

At each scale, the confidence parameter associated with the phase gradient estimation (C_f) and the coherence of interferogram ($C_\circ$) are combined as follows:

$$\mathbf{C}_\phi = \frac{C_f C_\circ}{1 - C_f - C_\circ + 2C_f C_\circ} \quad (1)$$

Then, a confidence parameter for each pixel after fusion of multiscale phase gradients is obtained by combining $\mathbf{C}_\phi$ at each scale according to Fig. 3b.

2.2.3 *Phase unwrapping*

The bi-dimensional approach used for phase unwrapping involves searching for a global solution by a least squares method. For this, *a priori* information available is the fused multiscale phase gradient and an associated confidence parameter. We search on the whole image for the unwrapped phase value, $\Phi(i, j)$, that minimises the squared error $\mathbf{E}$ defined as follows:

$$\mathbf{E} = \Sigma_{i=1}^{M-1} \Sigma_{j=1}^{N} C_\phi(i, j)(\Phi(i+1, j) - \Phi(i, j) - f_x(i, j))^2 + \Sigma_{i=1}^{M} \Sigma_{j=1}^{N-1} C_\phi(i, j)(\Phi(i, j+1) - \Phi(i, j) - f_y(i, j))^2 \quad (2)$$

where i and j represent the line and column index, respectively. The numbers of lines M and columns N are chosen as a power of 2 to speed up the discrete cosine transform algorithm used in the minimization.

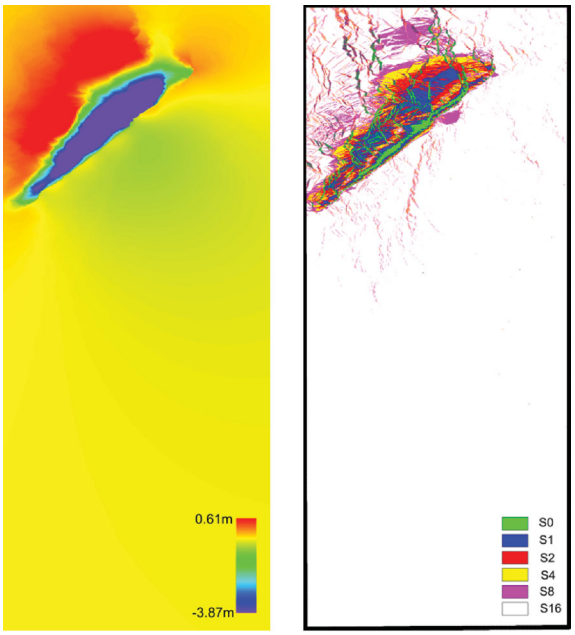

Figure 3. (a) *A priori* deformation model in line of sight (LOS) direction, negative value for displacement towards the satellite. It corresponds to the surface displacement predicted by an homogeneous elastic linear deformation model obtained from the coseismic slip distribution in Pathier *et al.* (2006). (b) Scale image for phase gradient estimation deduced from the *a priori* deformation model. S_0 corresponding to the full resolution SLC image and S_n to the multilooking image after a complex average of n looks in range and $5n$ looks in azimuth. All images are in the radar geometry of the track 463[1] (2004/11/06–2005/11/26).

2.2.4 *Multiscale adaptive filtering*

In order to validate the results of the phase unwrapping, we perform an adaptive filtering on the original differential interferograms (interferograms after topographic and orbital corrections) at scale S_2 using the multiscale phase gradients. The objective is not to recover the unwrapped phase directly, but to seek to eliminate the noise that affects the wrapped phase, then to bring out the fringe pattern. The phase signal is continuous only if it is analysed in complex form. The complex average of a great number of pixels, assumed independent, allows the variance of phase estimation to be reduced. On the basis of this principle, the original differential interferograms are filtered by multiscale phase gradients. Then they are compared with the re-wrapped unwrapped interferograms in order to quantify the residual of phase unwrapping. Only the interferograms whose

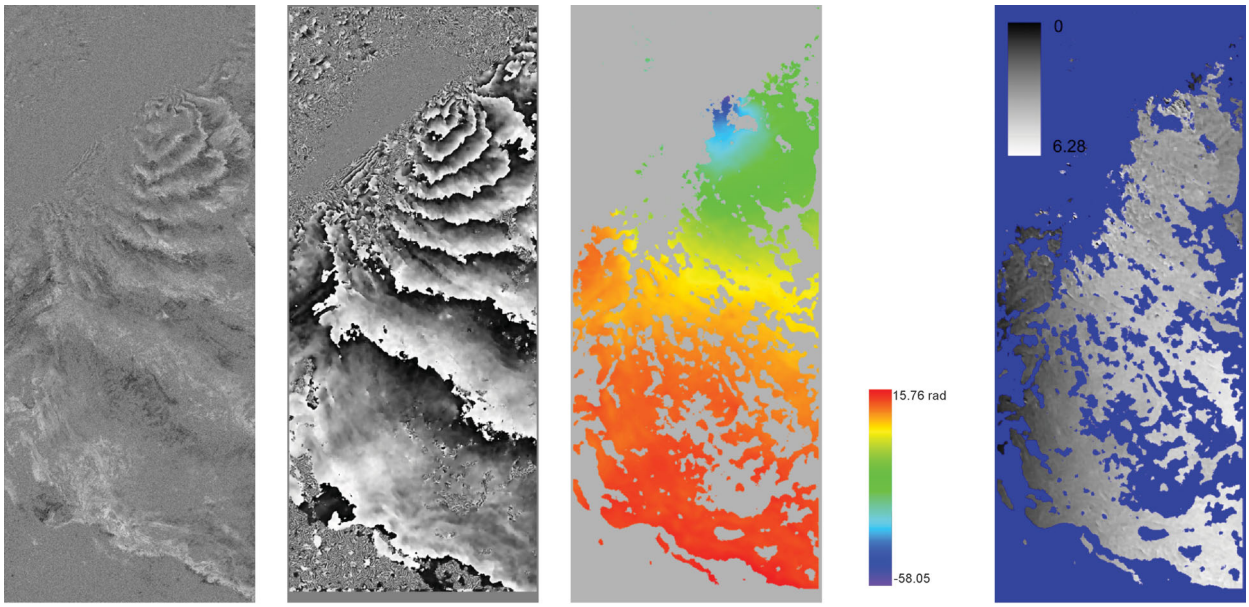

Figure 4. (a) Original differential interferogram (b) Filtered interferogram by multiscale phase gradient (c) Unwrapped interferogram using multiscale phase gradient by a least squares method (d) Wrapped phase residual. All images are at scale S_2 and in the radar geometry of the track 463[1] (2004/11/06–2005/11/26).

residual is inferior to 2π are considered as correctly unwrapped and used hereafter.

An example of the original differential interferogram, the filtered interferogram, the unwrapped interferogram and the wrapped residual interferogram for the track 463 (2004/11/06–2005/11/26) is shown in Fig. 4. With respect to Fig. 4(a), noise is greatly reduced in Fig. 4(b) and the fringe patterns are highlighted. In particular, some fringes near the fault are recovered successfully. In order to ensure the quality of phase unwrapping, a severe thresholding is performed on the confidence parameter associated with the estimated phase gradient. Consequently, some pixels are masked, especially near the fault (Fig. 4(c)). In the non-masked area, the wrapped residual is almost homogeneous and there is no presence of fringes (Fig. 4(d)), according to which the obtained phase values are considered to be unwrapped correctly.

2.2.5 *Atmospheric correction*

The atmospheric phase screen is one of the main factors that prevents the extraction of the displacement signal from interferograms (Zebker *et al.* 1997). It can be decomposed into a stratified part and a turbulent part. Regarding the turbulent component, it is considered to be spatially correlated but random in time, and can be removed by stacking interferograms or filtering (Schmidt and Bürgmann 2003; Hooper *et al.* 2007). Regarding the stratified component, it can be estimated from global atmospheric models which provide temperature and water vapour content along a given number of pressure levels (Doin *et al.* 2009).

Here we estimate the tropospheric phase delays using the ERA40 reanalysis from the European Centre for Medium-Range Weather Forecasts (ECMWF), which covers the studied period with a temporal resolution of 6 hr, a spatial resolution of 1.125° and provides values for 23 pressure levels.

For the phase delay calculation, we follow the methods described by Doin *et al.* (2009) and the average phase delay/elevation ratio τ, between the minimum and maximum elevations, $z_{\min}$ and $z_{\max}$, in each SAR scene is defined by:

$$\tau = \frac{\int_{z_{\min}}^{z_{\max}} \delta\phi(t1)\mathrm{d}z - \int_{z_{\min}}^{z_{\max}} \delta\phi(t2)\,\mathrm{d}z}{z_{\max} - z_{\min}} \tag{3}$$

where $t1$ and $t2$ denote the two acquisition dates.

The ratio estimated from ERA 40 is then compared with the ratio obtained from the linear correlation of the unwrapped phase and the elevation (Cavalié *et al.* 2007; Doin *et al.* 2009).

The D-InSAR measurements used in this paper, include four interferograms on descending pass and one interferogram on ascending pass. The agreement between interferogram derived ratio and atmospheric model derived ratio confirms the presence of topographically related atmospheric effects. Thereafter, we correct the topographically correlated atmospheric phase using the atmospheric model derived ratio on the interferograms where there is a good agreement. An example of the Track 191 is shown in Supporting Fig. S1.

2.2.6 *Determination of displacement reference*

As there is a constant shift on the unwrapped phase values, it is necessary to add or subtract a constant to the phase issued displacement values in order that the displacement values in the far field of the fault are close to 0. For this, we use the displacement values obtained from subpixel image correlation of the same image pair. Although the displacement values in the far field given by the subpixel image correlation are noisy, they provide an approximate measure of displacement. In particular, in the used measurements, the displacement differences between these two types of measurement are almost constant. This allows the referment of phase-issued displacement values by adding these differences.

2.2.7 *Estimation of phase uncertainty*

Because of the complexity of the processing chain, it is very difficult to quantify errors arising from data processing. In particular, without ground truth, it is impossible to estimate the error induced at the step of displacement reference determination. However, it is important to obtain a measure of uncertainty associated with the displacement. Therefore, we use coherence information to estimate the phase variance (σ_ϕ) due to noise present in the interferograms (Trouvé *et al.* 1998). This phase variance, which characterises essentially random variation of phase values, is used as uncertainty associated with displacement.

$$\sigma_\phi = \frac{1}{\sqrt{2M}} \frac{\sqrt{1-C_\circ^2}}{C_\circ} \tag{4}$$

with $C_\circ$ the coherence and M the number of multilooking, 40 in this study, since the unwrapped phase is issued from the combination of multiscale phases, from S_1 to S_{16}.

Finally, 23 sets of coseismic measurements including 18 sets from subpixel image correlation and 5 sets from D-InSAR are obtained (Table 1). Their spatial distribution is shown in Fig. 5. In particular, the spatial distribution of D-InSAR measurements is shown in Fig. 2.

3 THREE-DIMENSIONAL SURFACE DISPLACEMENT FIELD RETRIEVAL

3.1 Three-dimensional surface displacement field issued from radar measurements

From the 23 sets of measurements obtained in the previous section, the 3-D surface displacement is retrieved by a linear inversion in least squares sense. Results shown in Fig. 6(a) are in good agreement with those obtained by Pathier *et al.* (2006) on the basis of six sets of subpixel image correlation measurement. The associated uncertainty (Fig. 6(b)) is obtained by propagation of uncertainties associated with the measurements resulting from subpixel image correlation and D-InSAR through the inversion system in the least squares method.

According to Figs 5 and 6, a fault rupture, composed of two segments (Northern segment and Southern segment), is observed from the surface where the displacement gradient is very large. This fault rupture corresponds to a thrust with the hanging wall in the North-East and the footwall in the South-West. The displacement on the footwall is relatively uniform, whereas the displacement on the hanging wall is larger at positions closer to the fault rupture. Regarding the displacement on the hanging wall, a SW component

Table 1. 23 sets of measurement for coseismic displacement measurement of the 2005 Kashmir earthquake. Cor_{Rg} and Cor_{Az} denote the measurement in range and azimuth direction, respectively, from subpixel image correlation. ϕ denotes the measurement from D-InSAR. Data in bold correspond to the same data sets as used by Pathier *et al.* (2006). Measurements ϕ, Cor_{Rg} of the Tracks 463^1 and 499^1, Cor_{Az} of the Tracks 499^1 and 499^3 correspond to the selection of measurements used in Section 4.

Orbit direction	No. track	Acquisition date	$B_\perp$ (m)	B_t (year)	Measurement type
Descending	191	20041018–20051107	18.5252	1.0532	Cor_{Rg}, Cor_{Az}, ϕ
	234	20051006–20060608	−42.0326	0.6721	Cor_{Rg}, Cor_{Az}, ϕ
	463	20041106–20051126	−21.9210	1.0548	Cor_{Rg}, Cor_{Az}, ϕ
		20041106–20060311	12.1250	1.3470	Cor_{Rg}, Cor_{Az}, ϕ
		20040724–20051022	−52.8583	1.2445	Cor_{Rg}, Cor_{Az}
Ascending	270	**20050625–20051112**	**72.2857**	**0.3811**	Cor_{Rg}, Cor_{Az}, ϕ
	499	20050815–20051128	42.0463	0.2856	Cor_{Rg}, Cor_{Az}
		20050815–20060313	42.4986	0.5779	Cor_{Rg}, Cor_{Az}
		20050919–20051024	**−268.0392**	**0.0970**	Cor_{Rg}, Cor_{Az}

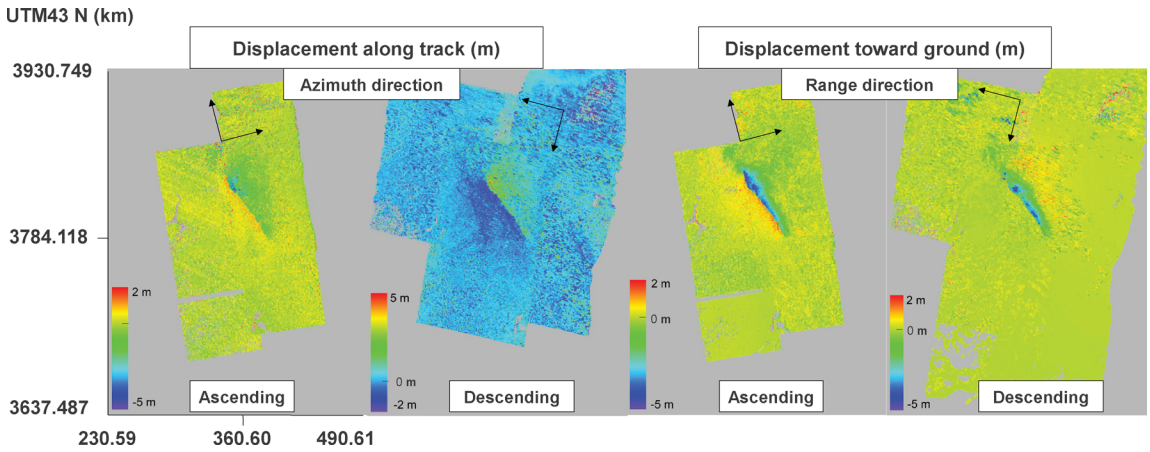

Figure 5. Coseismic displacement field obtained by fusion of subpixel image correlation and D-InSAR measurements. The location of each track is shown in Fig. 1. For each pixel, the displacement value corresponds to the displacement value whose associated uncertainty is the smallest among all of the available measurements. The colour discontinuity corresponds to the fault rupture.

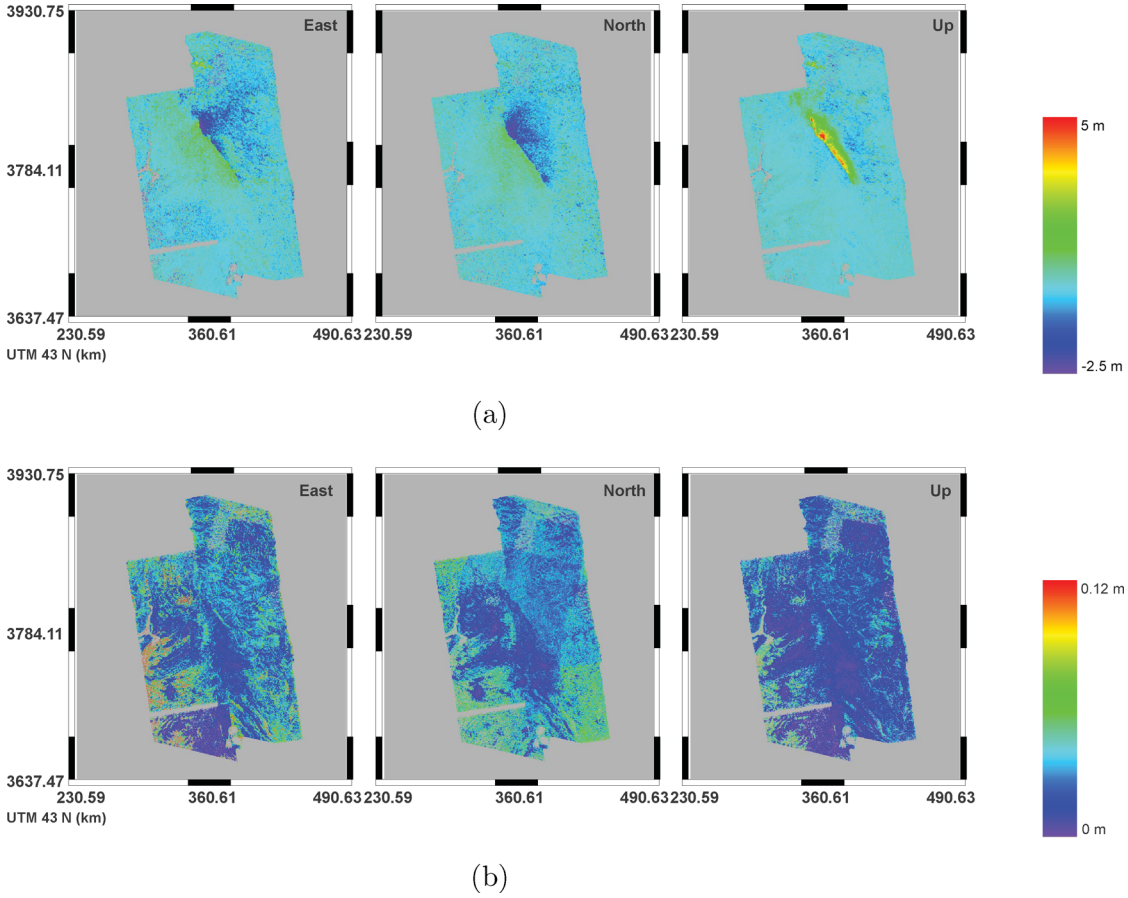

Figure 6. (a) 3-D surface displacement field, (b) associated uncertainty retrieved by a least squares inversion using 18 sets of subpixel image correlation measurement and five sets of D-InSAR measurement. The associated uncertainty is obtained by propagation of uncertainties associated with subpixel image correlation and D-InSAR measurements through the least squares inversion.

and a Up component are observed. Moreover, a progressive decrease of the West component from North to South along the fault trace is observed, which is consistent with the observation obtained by Pathier *et al.* (2006). These observations are consistent with the behaviour of the Bagh–Balakot fault reported by previous work: a pure thrust towards SW on the Northern segment and a significant increase of right lateral slip on the Southern segment on the hanging wall.

In addition to providing precise displacement information in the far field of the fault, another contribution of D-InSAR measurements to 3-D surface displacement retrieval relies on the reduction of the uncertainty associated with the displacement values according to comparisons performed between the case with D-InSAR measurements and the case without D-InSAR measurements (Yan *et al.* 2012).

3.2 Horizontal surface displacement issued from optical measurements

Two optical ASTER images acquired on 14 November 2000 and 27 October 2005, are used to retrieve the horizontal surface displacement by subpixel image correlation with COSI-Corr (Leprince *et al.* 2007). The images and methods are the same as used in Avouac *et al.* (2006). These two optical images are processed with objective to obtain a set of measurement independent of the radar measurements in order to perform a comparison between these two types of measurement. In order to measure the displacement along the fault trace, a series of profiles are created by averaging a band of pixels that is perpendicular to the fault trace. Then, the displacement on the fault is obtained by a linear regression on these profiles. The uncertainty associated with the displacement on the fault by the linear regression corresponds to the standard deviation of the regression on each side of the fault.

In order to facilitate the comparison in the following section, the same profiles are created on the horizontal displacement obtained from radar measurements along the fault trace.

3.3 Comparison of the surface displacement estimated by radar, optical and *in situ* measurements

As the vertical surface displacement along the fault trace has been measured on the field by Kaneda *et al.* (2008), three types of surface displacement measurement along the fault trace with completely different sources of information and data processing methods are available for this earthquake. The associated uncertainty is independent from one type of measurement to another. This allows the results issued from each type of measurement to be validated through inter-comparisons, since there is no other ground truth available. In this section, the horizontal displacements along the fault trace between the radar and optical measurements and the vertical displacements along the fault trace between the radar and *in situ* field measurements (Kaneda *et al.* 2008) are compared. The horizontal displacements along the fault trace obtained from both radar and optical measurements are shown in Fig. 7. A reasonable

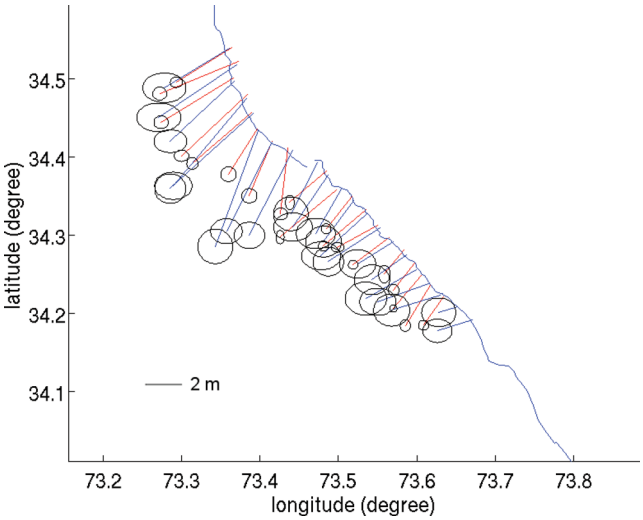

Figure 7. Horizontal displacement along the fault trace (red and blue vectors are, respectively, for radar and optical measurements). The ellipses represent the 2σ uncertainty.

general agreement is achieved, except in the Northern segment between longitude 73.35°E and 73.45°E, where a large discrepancy is observed. This discrepancy may be explained by uncertainties associated with each type of measurements.

The vertical displacements along the fault trace obtained from radar and *in situ* measurements are shown in Fig. 8. The displacement resulting from radar measurements corresponds to the upper boundary of the displacement resulting from *in situ* measurements. The difference is large and the variation of *in situ* measurements is significant. This can be explained by the fact that the *in situ* measurements are instantaneous point measurements, corresponding to the local deformation, and the total displacement could be underestimated if the displacement is distributed over a large area of several hundred meters, while the radar measurements are averaged in an area of about 20 pixels (∼2.4 km), plus low-pass filtering during data processing.

In order to analyse the uncertainty associated with the radar measurements, three pre-seismic pairs of SAR images, whose perpendicular and temporal baselines are similar or inferior to those of coseismic image pairs issued from the same track, are used (Table 2). According to these analyses, the maximum 3-D surface displacement error estimated from radar measurements is on the order of 0.2 m, which is consistent with the nominal uncertainty associated with the displacement measurement issued from subpixel image correlation of SAR images. Therefore, we decided to analyse the coseismic fault geometry and slip distribution inverting only radar measurements hereafter.

4 COSEISMIC FAULT GEOMETRY AND SLIP DISTRIBUTION INFERRED FROM SAR IMAGERY

The fault geometry parameters such as strike, dip, rake, slip, (X, Y) (the coordinate of the centre of the fault break at the Earth's surface in the East and North direction, respectively, in the UTM N43 projection system), length, depth and the slip distribution on the Balakot–Bagh fault have been retrieved by inversion of a homogeneous, elastic, half-space mechanical deformation model (Okada 1985) using subpixel SAR image correlation measurements (Pathier *et al.* 2006; Wang *et al.* 2007), optical measurements and teleseismic waveform (Avouac *et al.* 2006). In this paper, we follow the same approach as used by Pathier *et al.* (2006): a nonlinear optimization of the fault geometry parameters assuming a uniform slip on the fault plane followed by a standard kinematic inversion for slip distribution with the previously optimized fault geometry parameters. However, the retrieval of the fault geometry parameters and the slip distribution are performed using measurements with larger spatial coverage (Fig. 1), especially using D-InSAR measurements that provide precise and continuous displacement information in the far field of the fault (Fig. 2). Moreover, in addition to the one segment slip model as in Pathier *et al.* (2006), a two segments slip model linked better to the surface fault break is proposed.

The data sets are downsampled using a quadtree algorithm with the objective being to keep as much as possible of the displacement variation information, but not to burden the inversion system. The split of the quadrant depends on the displacement variance within the quadrant. The threshold of the displacement variance is chosen based on the trade-off between the number of points and the displacement variation. If the displacement variance in a given quadrant is smaller than the threshold, the median value of displacements is taken for this quadrant; otherwise, the quadrant is split into four subquadrants. The improvement by taking the median value of displacements is discussed in Dawson & Tregoning (2007). An example of the quadtree downsampling is shown in Supporting Fig. S2.

First of all, the fault geometry parameters and the slip distribution are retrieved by using all of the available measurements. Then, a selection of measurements (five sets of D-InSAR measurement and four sets of subpixel correlation measurement (Table 1)) whose residual (difference between the data observation and the model

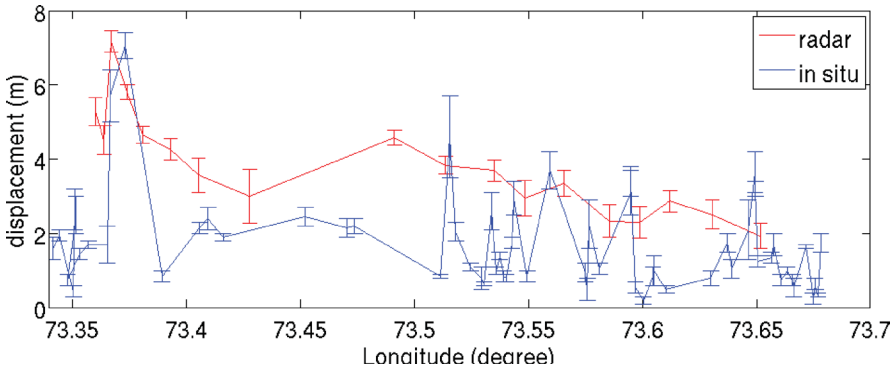

Figure 8. Vertical displacement along the fault trace (*in situ* field measurements in blue and radar measurements in red).

Table 2. Available data sets for pre-seismic displacement measurement of the 2005 Kashmir earthquake. Cor_{Rg} and Cor_{Az} denote the measurement in range and azimuth direction, respectively, from subpixel image correlation. ϕ denotes the measurement from D-InSAR.

Orbit direction	No. track	Acquisition date	$B_\perp$ (m)	B_t (year)	Measurement type
Descending	463	20040306–20041106	4.0353	0.6667	Cor_{Rg}, Cor_{Az}, ϕ
Ascending	270	20050730–20050903	43.5286	0.0927	Cor_{Rg}, Cor_{Az}, ϕ
	499	20050502–2005091 9	−19.8367	0.3799	Cor_{Rg}, Cor_{Az}, ϕ

Table 3. Fault geometry parameters of the one segment slip model.

Strike (°)	Dip (°)	Rack (°)	Slip (m)	X (km)	Y (km)	Length (km)	Depth (km)
320.37	38.96	98.22	4.84	364.29	3797.81	68.33	13.22

Table 4. Fault geometry parameters of the two segments slip model.

–	Strike (°)	Dip (°)	Rack (°)	Slip (m)	X (km)	Y (km)	Length (km)	Depth (km)
South segment	320.37	39.92	105.14	4.30	371.07	3789.65	60	14.12
North segment	343	39.92	152.18	3.21	349.60	3820.41	16	8.64

prediction) is less than 0.5 m is used to estimate the fault geometry parameters and the slip distribution. According to the results obtained, these two approaches give almost the same results, but using the selection of measurements is much less time consuming. Consequently, further analyses are performed with this selection of measurements.

4.1 Fault geometry parameters

The obtained fault geometry parameters for the one segment slip model are shown in Table 3. They are consistent with the results obtained by Pathier *et al.* (2006), Avouac *et al.* (2006) and Kaneda *et al.* (2008), as well as with the Harvard CMT solution (determined from the modelling of the long-period surface wave) and the focal mechanism determined by the USGS from teleseismic waves.

Regarding the retrieval of the fault geometry parameters for the two segments slip model, the intersection point of the two segments at the Earth's surface, the strike, the length and the (X,Y) of each segment are determined from the surface fault break and they are fixed in the inversion, on the one hand in order that the two segments model is better lied to the surface observation of the fault rupture, on the other hand in order to facilitate the optimization of the fault geometry parameters. The obtained fault geometry parameters for the two segments model are shown in Table 4. Globally, they are consistent with the parameters of the one segment model. They are also consistent with the parameters of the two segments model in Avouac *et al.* (2006).

4.2 Slip distribution

There are some differences more or less significant between the slip distributions obtained by different authors (Avouac *et al.* 2006; Parsons *et al.* 2006; Pathier *et al.* 2006). Two major slip asperities are identified in the Northern segment (Balakot–Muzaffarabad) and the Southern segment (Muzaffarabad–Bagh) by Pathier *et al.* (2006) and Parsons *et al.* (2006): the one in the Northern segment is a larger-slip asperity, whereas the one in the Southern segment is a smaller-slip asperity. Moreover, they are consistent with the surface slip distribution obtained by Kaneda *et al.* (2008). However, the ones in the Southern segment inferred by Parsons *et al.* (2006) and Kaneda *et al.* (2008) have a larger size than the one inferred by Pathier *et al.* (2006). Furthermore, the centre of the Northern asperity is located further North by Parsons *et al.* (2006) than by Pathier *et al.* (2006). Avouac *et al.* (2006) suggest a single asperity just above the hypocenter, assuming a fault with two segments. Additionally, the zone with the maximum slip is located further South than in the slip distribution derived by Pathier *et al.* (2006).

To estimate the slip distribution, a Laplacian smoothing is used in the inversion to avoid the oscillation (Hsu *et al.* 2002; Yu *et al.* 2003; Funning *et al.* 2005; Pathier *et al.* 2006). In this paper, the smoothing factor is chosen based on the trade-off between the roughness of the model and the rms. The obtained one segment slip distribution model is shown in Fig. 9 (see detailed text file s2005Kashmirarche_1seg.slp in Supporting Information). The seismic moment related to this slip distribution is 2.99×10^{20} N m, very close to the Harvard CMT solution (2.94×10^{20} N m). Two major slip asperities are observed. Beneath the Northern segment, occurred the slip larger than 6 m with a peak of 9 m at 6 km depth (deeper than in Pathier *et al.*, 2006). Beneath the Southern segment, smaller slip occurred with a maximum of 7 m at 4 km depth. Furthermore, in the Northern segment, our slip distribution shows larger slip at depth than other models, which can be explained by the different spatial coverage of data used in this paper, especially the far field data. The two segments slip distribution model is shown in Fig. 10 (see detailed text file s2005Kashmirarche_2seg.slp in Supporting Information). The seismic moment related to this slip distribution is 2.87×10^{20} N m, also close to the Harvard CMT solution. At the intersection of the two segments, the transition of slip values is not perfect because of the edge effect on each segment. Regardless of this effect, two major slip asperities can be considered, which is consistent with the one segment slip model. Compared to the one segment model, globally the slip is larger on both Northern and Southern segments. The Northern segment fits the surface fault rupture better. The size of the Northern asperity is larger, while the size of the Southern asperity is smaller and shallower. By comparison with the two segments model in Avouac *et al.* (2006), the two asperities in our model correspond better to the surface slip distribution, especially on the Southern segment. At the end of both Southern and Northern segments, the slip is larger but shallower in our model. Also, the Northern asperity in our model is deeper than the major asperity in Avouac *et al.* (2006). The obtained results confirm the occurrence of larger slip along the Northern part of the thrust. This larger coseismic slip induces a larger post-seismic

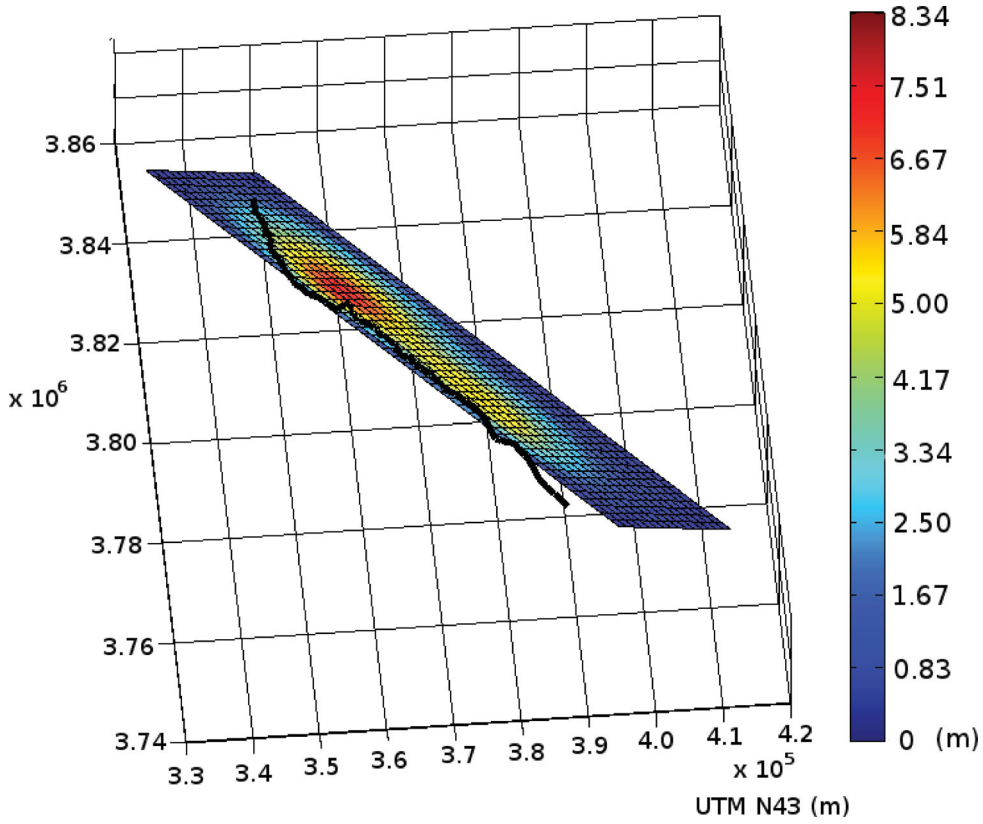

Figure 9. One segment slip model. The fault rupture at surface is marked by the black line.

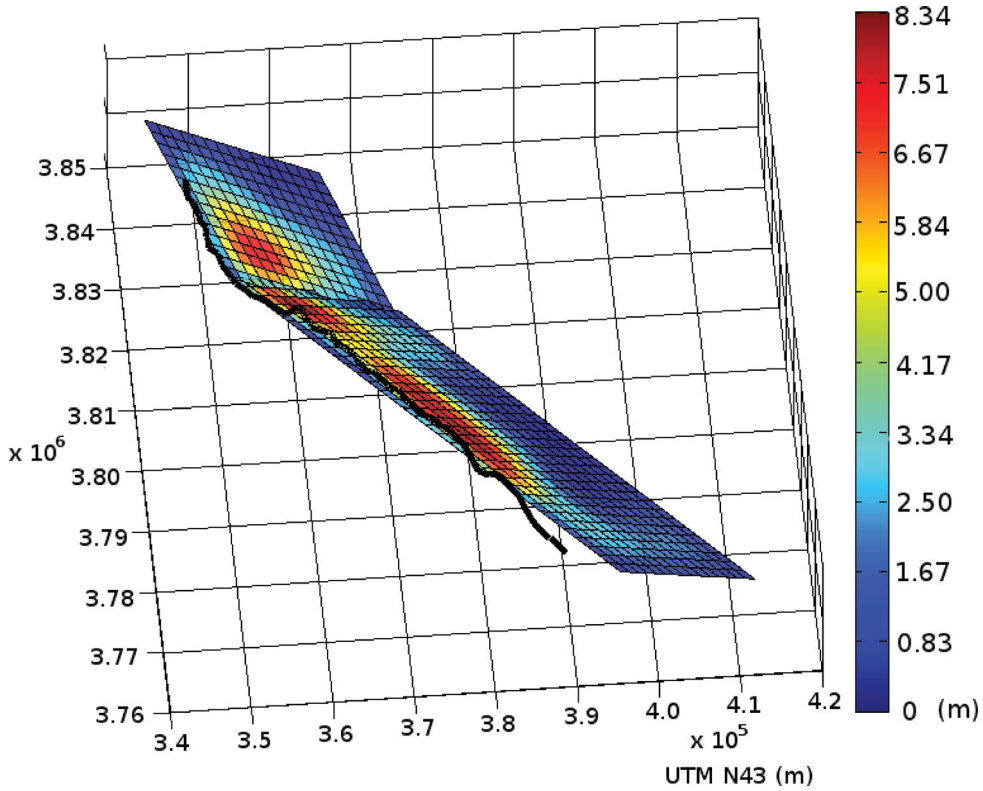

Figure 10. Two segments slip model. The fault rupture at surface is marked by the black line.

slip along the part of the ramp following the Northwestern segment (Jouanne *et al.* 2011). The asymmetry of co- and post-seismic slip between the Northwestern segment and the Southeastern segment is also illustrated by the spatial distribution of aftershocks, these ones being mainly located NW of the thrust (Jouanne *et al.* 2011).

4.3 Residual analysis

The residuals of both slip models are calculated for each data set in order to further evaluate the obtained slip models. For this, the 3-D displacement field is constructed from the slip distribution model, and then projected into the direction of each data set and compared to the original data set. The residuals (model minus data) for some data sets are shown in Figs 11–14.

Firstly, the residuals of subpixel correlation data sets are discussed. For the data set of Track 499[3] (Cor_{Az}) (Fig. 11), there is a good agreement between the data and the two models, except that at the end of the Southern segment, a small area with large residual is observed with both models. This small area corresponds to the positions where there is a discrepancy between the modelled fault trace and the observed fault trace (Figs 9 and 10). The improvement of the two segments model is not significant regarding the residual. However, by comparison of the displacement field issued from two models, the displacement field issued from the two segments model is clearly more similar to the data observation. Regarding the data set of Track 463[1] (Cor_{Rg}) (Fig. 12), there is a great difference between the two models in interpreting the data. A good agreement is obtained between the data and the two segments model.

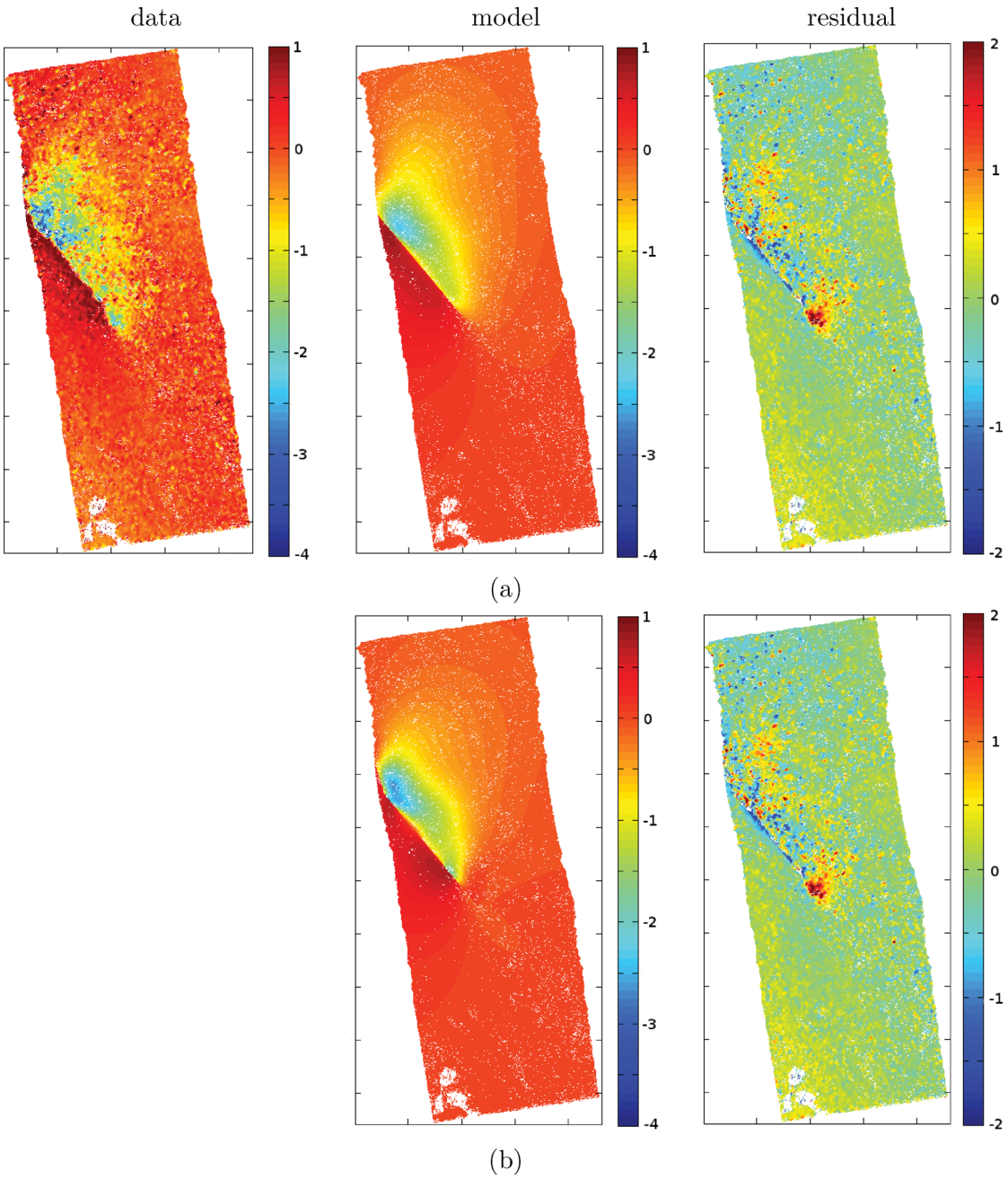

Figure 11. Residual of the Track 499[3], Cor_{Az} (model minus data). (a) one segment model (b) two segments model.

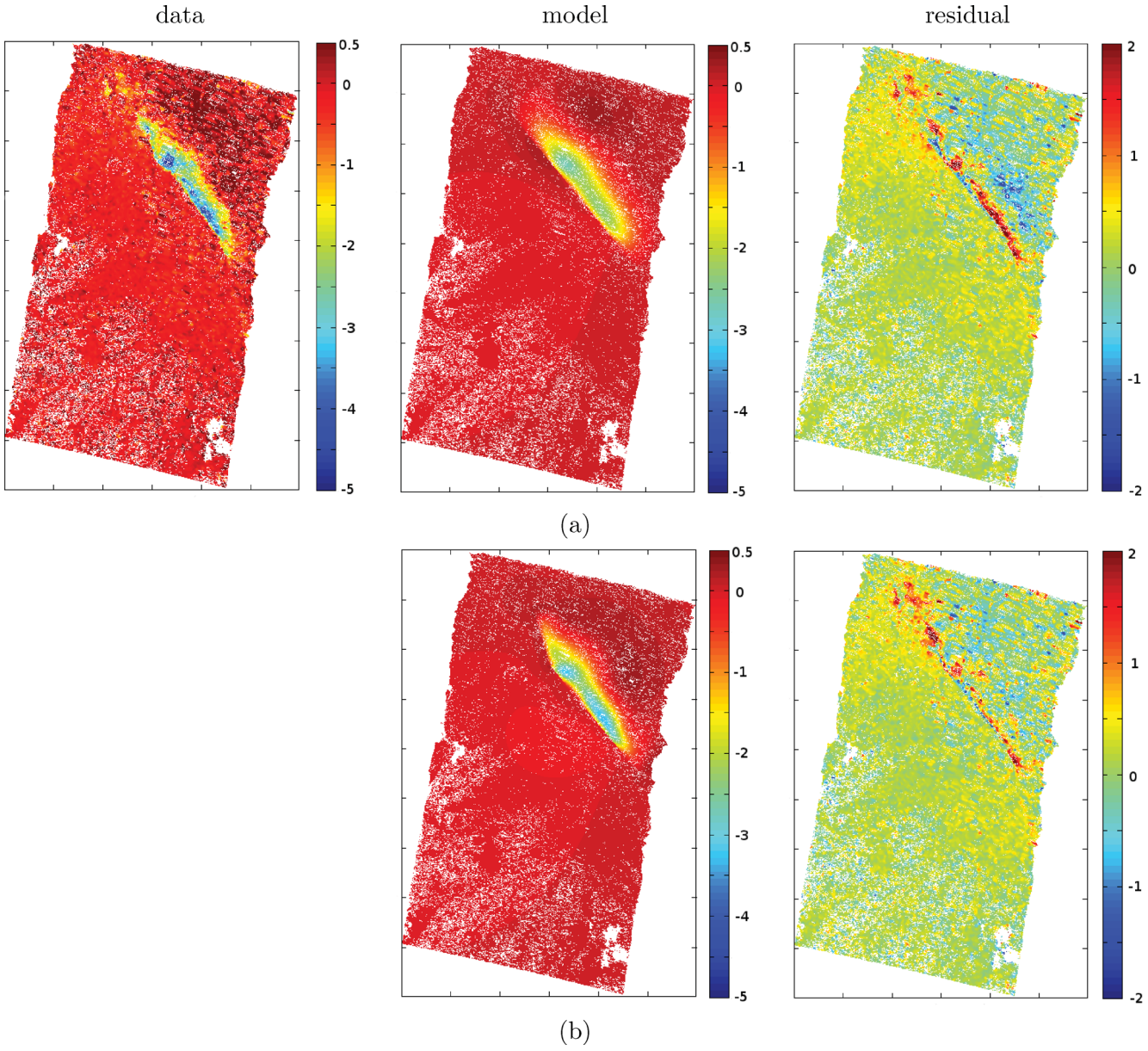

Figure 12. Residual of the Track 463[1], Cor_{Rg} (model minus data). (a) one segment model (b) two segments model.

However, for the one segment model, the displacement field with strong magnitude near the fault on the hanging wall given by the model is more regular and smaller than that observed from the data, which causes the significant difference on the order of 2 m near the fault on the hanging wall in the Southern part. This observation indicates slip deficit in this area. Moreover, on the hanging wall, further NE far from the fault, the model presents an excess of displacement, which implies that the Southern asperity should be shallower than that in the one segment model. Regarding the displacement field issued from two models, the displacement field issued from the two segments model is more similar to the data observation. Therefore, the two segments model clearly interprets the data better than the one segment model according to this data set.

In fact, the subpixel correlation data sets allow only the displacement field on the fault and near the fault predicted by the slip model to be validated, since they cannot capture the detailed displacement information in the far field because of the limitation of the technique precision. The difference in detail in the far field on the hanging wall as well as in the near field on the footwall where the displacement magnitude is small, cannot be observed from these residuals. This indicates the need to use far field precise and continuous data in order to further evaluate the obtained slip models.

Secondly, the residuals of D-InSAR data sets are discussed. For the data set of Track 191 (φ) (Fig. 13), the residual is small for both models, but a slight tilt effect is observed, which indicates the gradient of the modelled displacement does not follow exactly that of the measured displacement, especially in the southern part of the footwall. This can be partly explained by the spatial distribution of points after the quadtree downsampling, since a few points are taken in this part because of the small variation of displacement values (Fig. S2). From comparison of the residuals of both models, no great improvement of the two segments model is observed, since the residual for both models is small. For the data set of Track

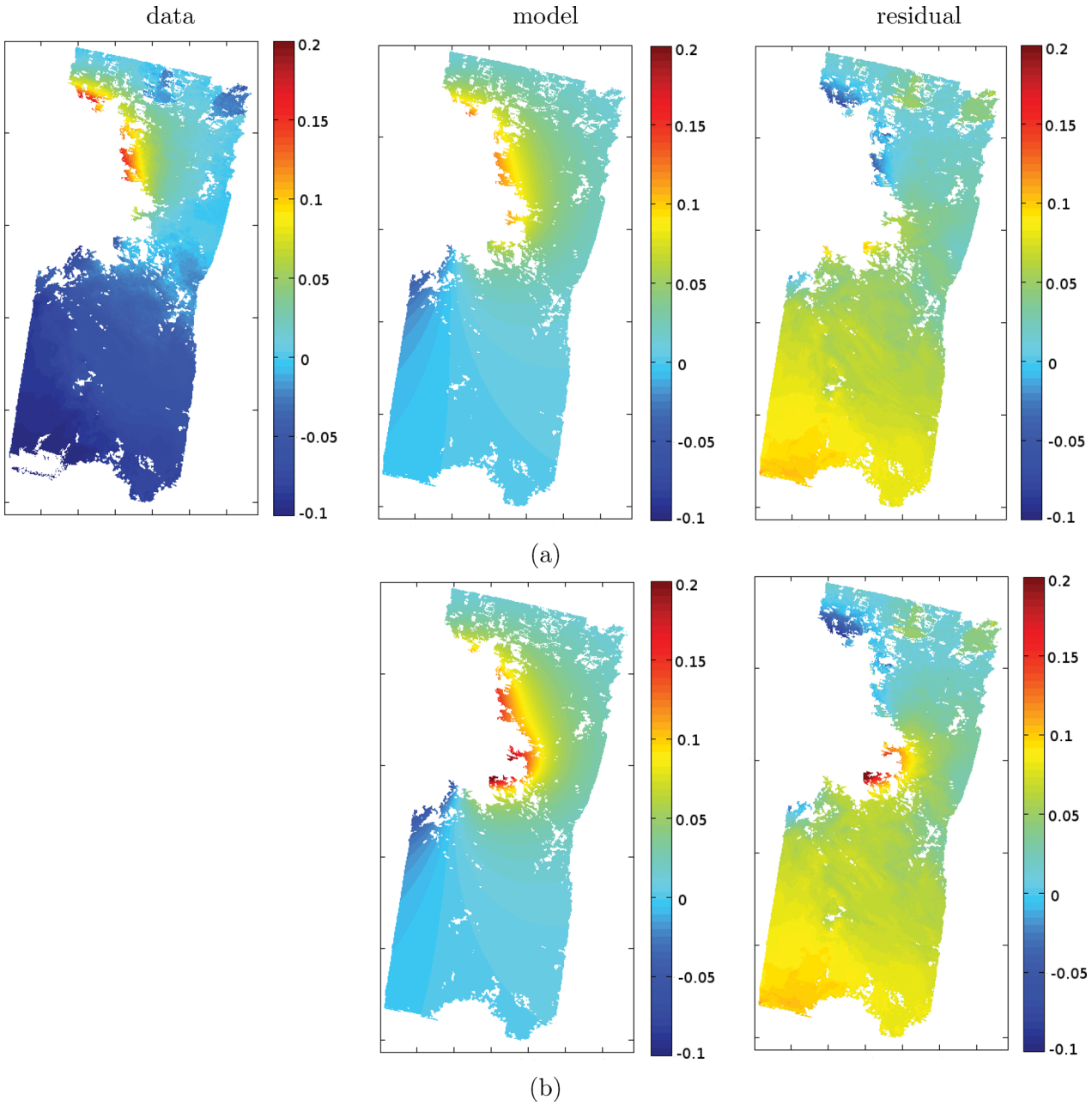

Figure 13. Residual of the Track 191, φ (model minus data). (a) One segment model (b) two segments model.

463^1 (φ) (Fig. 14), the data essentially cover the footwall. The two models present slip deficit on the footwall of the Northern segment, where relatively large residual is observed. These observations are consistent with the observations of the residual of the subpixel correlation data set of the same Track (463^1 Cor_{Rg}). On the Northern segment, relatively large residual is observed on the hanging wall, which indicates slip deficit on this segment (Fig. 12). In both data sets, the residual is smaller for the two segments model. With the two segments model, the modelled fault geometry fits better the observed surface fault rupture. However, the Northern slip asperity is perturbed by the segments' intersection, therefore, slip deficit still exists, despite of the improvement with respect to the one segment model.

According to these analyses, we can conclude that the two segments slip model can explain the displacement field measured by the data in the near field and in the far field of the fault at the same time in a satisfactory manner. Adding D-InSAR data that provide precise continuous displacement information, especially in the far field, allows the slip models to be better constrained and validated. Although the one segment slip model is not as good as the two segments slip model in interpreting the data observation, the validation of the one segment slip model by D-InSAR measurement is important, since the one segment slip model obtained in this paper is consistent in general with the one segment slip models obtained in previous work, but there was not such detailed validation performed in previous work.

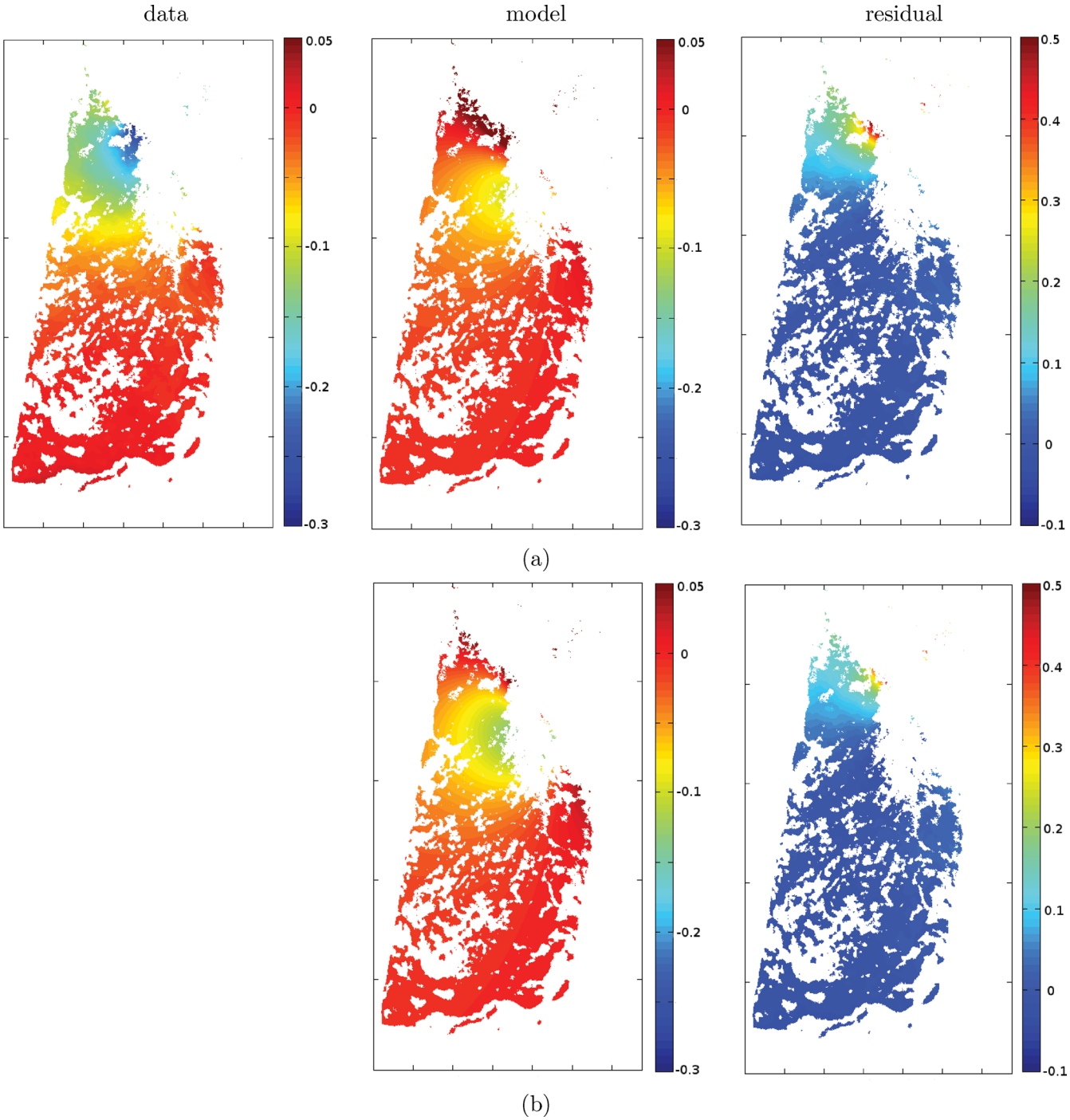

Figure 14. Residual of the Track 463[1], φ (model minus data). (a) one segment model (b) two segments model.

5 INVESTIGATION OF WEDGE THRUST AND POTENTIAL SLIP ALONG A DÉCOLLEMENT LEVEL

5.1 Investigation of wedge thrust

In Bendick *et al.* (2007), a wedge thrust, including a NNE dipping fault plane extending WNW from Balakot and an intersecting nearly flat dislocation at ∼5 km depth, is inferred from the historical regional seismicity, aftershock distribution and aftershock focal mechanism in addition to a main rupture as estimated by Pathier *et al.* (2006); Parsons *et al.* (2006). The GPS measurements are used to constrain the slip magnitude on the wedge thrust. Since the data used by Bendick *et al.* (2007) are located NW of the main rupture terminating at Balakot along the Indus Valley, the question arises whether the displacement observed by Bendick *et al.* (2007) is linked essentially with the strong aftershocks occurred in this area, not with the main shock. On the other hand, according to the residual analysis of our slip models, relatively large residual is observed in and to the NW of the Balakot–Muzaffarabad segment

Table 5. Geometry parameters of the wedge thrust modified from Bendick *et al.* (2007) in order to fit our two segments model. Parameters in bold correspond to modified parameters.

Strike (°)	Dip (°)	Rack (°)	Slip (m)	X (km)	Y (km)	Length (km)	Depth (km)
320.37	**39.92**	90	1.8	**328.04**	**3843.10**	44	5–20

(Figs 12 and 14), thus the question arises if this wedge thrust can explain this large residual. Moreover, it makes sense that there is a fault to the NW of the Balakot–Muzaffarabad segment that ensures the continuity of the Balakot–Bagh fault and the Indus Kohistan Seismic Zone. Consequently, the test of wedge thrust is performed with the data sets used in this paper.

Since the geometry of the wedge thrust in Bendick *et al.* (2007) is consistent with the geometry of the one segment model estimated by Pathier *et al.* (2006); Parsons *et al.* (2006), it is not consistent with our two segments slip model geometry. In the data sets used in this paper, only several subpixel image correlation measurements cover the NW part where most of the aftershocks are located, we cannot constrain directly the wedge thrust using these data sets. Therefore, the geometry of the wedge thrust in Bendick *et al.* (2007) is slightly modified in order that it fits our two segments model and follows the Northern segment in the Northwest. The geometry parameters of the modified wedge thrust is shown in Table 5. The displacement field induced by this two segments main rupture plus wedge thrust model is obtained by adding the displacement field induced by this wedge thrust, calculated using uniform slip (the same as in Bendick *et al.* (2007)), to the displacement field induced by the two segments fault. The residuals of the two segments main rupture plus wedge thrust model with respect to both the subpixel correlation and the D-InSAR data sets of the Track 463[1] are shown in Fig. 15.

Comparing Fig. 15(a) and 12, the residual is slightly reduced to the NW of the Balakot–Muzaffarabad segment. However, a small excess of displacement appears further NW, which can be observed from the residual in blue in Fig. 15(a). Comparing Fig. 14 and 15(b), no observable difference is obtained between these two residuals. On the one hand, these observations confirm that the residual in this area is mainly due to the slip deficit of the two segments model on the Northern segment. On the other hand, the wedge geometry in this test is determined in an arbitrary way based on the wedge geometry proposed by Bendick *et al.* (2007) and the geometry of our two segments model. Moreover, the slip on the wedge is assumed to be uniform. If such a wedge thrust dose exist, the imprecise information of the geometry and slip in this test may perturb the real contribution of the wedge thrust to the coseismic displacement interpretation. Even so, we can observe that in this test the model with wedge thrust reduces slightly the residual to the NW of the Balakot–Muzaffarabad segment. Therefore, further investigation is necessary in order to constrain a wedge thrust that corresponds to the two segments slip model and to discuss its contribution to interpreting the measured displacement field.

5.2 Investigation of potential slip along a décollement level

According to Jouanne *et al.* (2011), post-seismic displacement measured by GPS campaigns, indicates an afterslip along a décollement located North of the ramp and connected to it. The slip along the NW portion of the décollement reached about 30.8 cm between November 2005 and August 2006. Due to coherence loss, this post-seismic displacement could not be detected in the post-seismic interferogram. However, the time span of the radar measurements used in this paper for coseismic analysis includes the post-seismic period (Fig. 16).

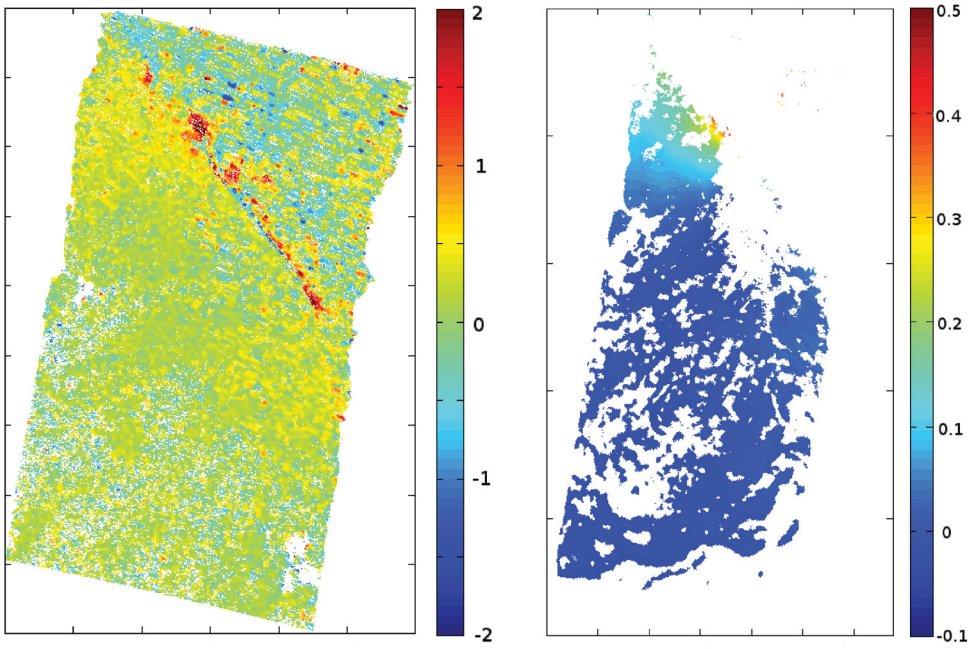

Figure 15. Residual (model minus data) of the model with wedge thrust with respect to (a) subpixel image correlation data set (b) D-InSAR data set of the Track 463[1]. The model used here is the combination of the two segments main rupture model proposed in this paper and a modified wedge thrust from Bendick *et al.* (2007).

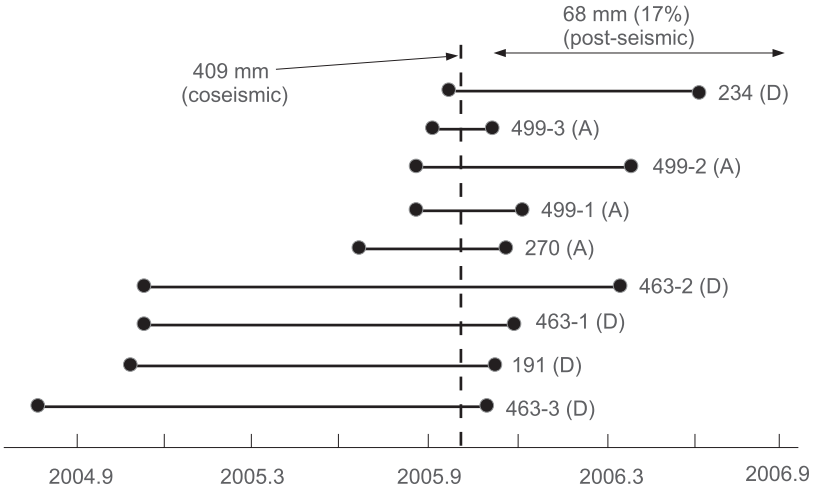

Figure 16. Temporal distribution of coseismic data sets versus post-seismic period. A denotes ascending pass and D denotes descending pass. The coseismic NS displacement (409 mm) derived in this study and the post-seismic NS displacement (68 mm, about 17 per cent of the coseismic displacement) at the position PS08 (see Fig. 1) between November 2005 and August 2006 from Jouanne *et al.* (2011) are indicated.

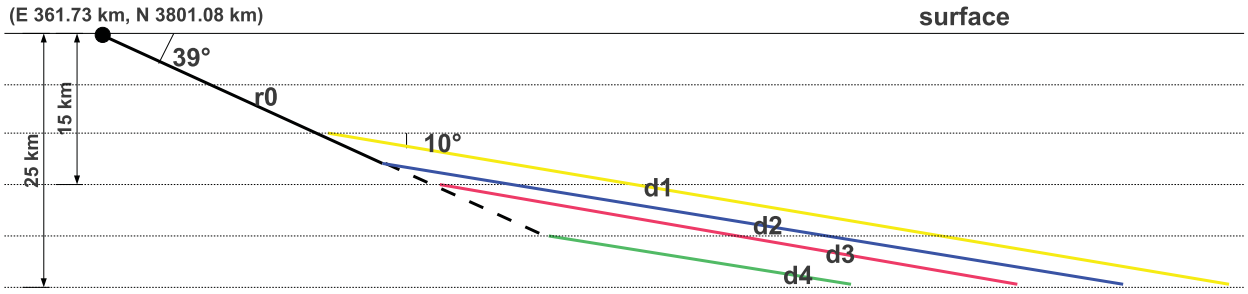

Figure 17. Geometry of the décollement in different configurations. Orientation N320. r0 represents the ramp. d1–d4 represent the four décollement configurations.

In order to understand how post-seismic slip along the décollement could affect the coseismic slip distribution derived from the data sets used in this paper, synthetic tests are realised. According to Jouanne *et al.* (2011), the ramp affected by the main shock is followed by a décollement with a dip angle of about 10° and situated at about 10–25 km depth. To quantify the displacement induced by the slip along this décollement in the coseismic data, two fault models are considered:

(i) model 1: a single ramp (r0) located between 0 and ∼13 km depth.

(ii) model 2: a ramp (r0) followed by a décollement (d1–d4). The data sets used in this paper cannot constrain the depth of the décollement, four configurations corresponding to four different locations of the décollement are tested (Fig. 17).

(a) d1: the décollement is located between 10 and 25 km depth and intersects the ramp.

(b) d2: the décollement is located between 13 and 25 km depth and connected to the ramp.

(c) d3: the décollement is located between 15 and 25 km depth without connexion to the ramp.

(d) d4: the décollement is located between 20 and 25 km depth without connexion to the ramp.

Since the data sets used in this paper cannot constrain the depth of the décollement, we cannot infer the geometry parameters of the décollement together with the geometry parameters of the ramp in one inversion. From the geometry parameters of the ramp and the geometric relationship between the ramp and the décollement, we deduce certain parameters of the décollement, such as top, (X, Y). The other parameters, like strike, rake, slip and length, are assumed to be the same as those of the ramp. Then the 3-D surface displacement field induced by the slip along the décollement is calculated using the forward model (Okada 1985). Afterwards, the 3-D surface displacement field induced by the slip along the décollement and that induced by the slip on the ramp are combined linearly in order to obtain the total 3-D surface displacement field. The latter (model prediction) is compared to the 3-D displacement field obtained directly by linear inversion of the radar measurements (data observation). In order to reduce noise, the comparison is performed on a profile averaged over a 151 pixels large band (Supporting Fig. S3).

The measured displacement is the sum of the displacement induced by the slip on the ramp and the displacement induced by the slip along the décollement plus random noise. However, the amount of slip on the décollement is unknown. In these tests, a unitary slip is considered on the ramp, as well as along the décollement. In order to determine the proportion of slip on the décollement with respect to that on the ramp, two coefficients are assigned to the surface displacement induced by the slip on the ramp and to the surface displacement induced by the slip along the décollement, respectively (eq. (5)). Thus, these two coefficients indicate the amount of slip on the ramp and on the décollement, respectively.

$$d_{\text{data}} = c1 * d_{\text{ramp}} + c2 * d_{\text{decollement}} + d_{\text{noise}} \quad (5)$$

Table 6. Coefficients $c1$, $c2$, rms and AIC values for different ramp/décollement configurations.

–	Model 1	Model 2			
–	r0	r0+d1	r0+d2	r0+d3	r0+d4
c1	4.9503	4.5022	4.4330	4.3812	4.1252
c2	0.0000	0.2483	0.3247	0.3828	0.6708
rms (m)	0.2746	0.2718	0.2713	0.2710	0.2705
AIC	2.2746	4.2718	4.2713	4.2710	4.2705

$c1$ and $c2$ are obtained by minimizing the root mean square (rms) that is defined below:

$$\text{rms} = \sqrt{\frac{\sum_i^I (d_{\text{data}}(i) - c1 * d_{\text{ramp}}(i) - c2 * d_{\text{decollement}}(i))^2}{I}} \quad (6)$$

with i index of pixel and I number of pixels on the profile.

The coefficients $c1$, $c2$ and the rms in different configurations are shown in Table 6. The values of $c2$ are much smaller than those of $c1$ for model 2. The values of $c1$ for model 2 vary slightly from one configuration to another. Moreover, they are close to the value for model 1. The differences of rms between model 1 and model 2 are extremely small, on the order of 0.1 cm. All these observations indicate that the best adjustment of model 2 is almost equivalent to that of model 1.

In order to further compare the two fault models, which imply a different number of parameters (one for model 1 and two for model 2), the Akaike information criterion (Akaike 1974) is used.

$$\text{AIC} = \chi^2 + 2n \quad (7)$$

where n is the number of parameters in the model and χ^2 corresponds to the rms.

Different AIC values are shown in Table 6. The AIC value for model 1 is much smaller than those for model 2. Therefore, we can conclude that the model with décollement cannot better explain the data observation, thus no slip along the décollement level can be detected in the used coseismic measurements.

The detection threshold of the slip on the décollement is estimated in the shallowest configuration (d1). If the slip on the décollement is inferior to 72.6 cm, it is difficult to distinguish the displacement induced by the slip along the décollement from the noise present in the radar measurements. Furthermore, the maximum slip on the décollement found by Jouanne *et al.* (2011) is about 30.8 cm. Therefore, we can conclude that the influence of the post-seismic displacement on the coseismic analysis is negligible.

To summarise, although the coseismic data used in this paper includes the post-seismic period, the coseismic displacement field and slip distribution are not significantly biased by the post-seismic slip that probably exists along the décollement, since even if it exists, the magnitude is small, less than 72.6 cm. If coseismic slip occurs on the décollement level, it must be small, less than 42 cm; otherwise, together with the post-seismic slip (∼30.8 cm maximum), it would be detected in the radar measurements. This evidence confirms the conclusion that the afterslip, driven by the stress change due to the main shock, affects mainly the décollement part which is not affected during the main shock.

6 CONCLUSION

A series of ENVISAT SAR images are processed to estimate the coseismic surface displacement due to the 2005 Kashmir earthquake. In particular, D-InSAR is applied to measure the surface displacement induced by this earthquake with success for the first time, thanks to the particular phase unwrapping chain developed in this study. The comparisons of surface displacement obtained from radar, optical and *in situ* measurements are performed. A satisfactory general agreement is obtained.

The coseismic fault geometry parameters and slip distribution are estimated using radar measurements, particularly the precise far field D-InSAR data. The obtained results are consistent with those obtained previously. In addition to the one segment slip model as proposed by most authors, a two segments slip model that better fits the surface fault break is prefered here. The slip models obtained are further evaluated by residual with respect to the data observation. Due to the D-InSAR data that provide precise displacement information in the far field of the fault, the performance of the slip models obtained in this paper is assessed in detail. The improvement in interpreting the measured displacement field of the two segments model is highlighted.

The wedge thrust proposed by Bendick *et al.* (2007) is tested. According to the residual analysis, it is possible that such wedge thrust exists, but the large residual observed in and to the NW of the Balakot–Muzaffarabad segment is mainly due to the slip deficit on the Northern segment in our slip models. Further investigation is necessary to constrain a wedge thrust that fits the two segments slip model and to discuss its contribution to interpreting the observed displacement field.

Although the coseismic data used in this paper include the post-seismic period, the magnitude of the post-seismic slip, revealed by GPS data on the décollement level, is so small that it cannot be detected by these coseismic data. Therefore, the coseismic slip distribution and displacement estimation are not significantly influenced by the post-seismic displacement.

ACKNOWLEDGMENTS

This work was supported by the EFIDIR project (http://www.efidir.fr) (ANR-07-MDCO-004) and the PAKSIS program CATTELL, granted by the French National Agency (ANR). The authors wish to thank the ANR for their support. The ENVISAT data are available thanks to ESA project category 1, No. 3802.

REFERENCES

Akaike, H., 1974. A new look at the statistical model identification, *IEEE Trans. Automat. Contr.,* **19**(6), 716–723.

Avouac, J., Ayoub, F., Leprince, S., Konca, O. & Helmberger, D.V., 2006. The 2005, M_w7.6 Kashmir earthquake: sub-pixel correlation of ASTER images and seismic waveforms analysis, *Earth planet. Sci. Lett.,* **19**(3–4), 514–528.

Bendick, R., Bilham, R., Khan, M. & Khan, S., 2007. Slip on an active wedge thrust from geodetic observations of the 8 October 2005 Kashmir earthquake, *Geol. Soc. Am.,* **19**(3), 267–270.

Bilham, R., Blume, F., Bendick, R. & Gaur, V., 1998. Geodetic constraints on the translation and deformation of india: implications for future great himalayan earthquakes, *Curr. Sci.,* **19**(3), 213–229.

Casu, F., Manconi, A., Pepe, A. & Lanari, R., 2011. Deformation time-series generation in areas characterized by large displacement dynamics: the SAR amplitude pixel-offset SBAS technique, *IEEE Trans. Geosci. Remote Sens.* **49**(7), 2752–2763.

Cavalié, O., Doin, M., Lasserre, C. & Briole, P., 2007. Ground motion measurement in the lake Mead area, Nevada, by differential synthetic aperture radar interferometry time series analysis: probing the lithosphere rheological structure, *J. geophys. Res.,* **112**(B03403), doi:10.1029/2006JB004344.

Dawson, J. & Tregoning, P., 2007. Uncertainty analysis of earthquake source parameters determined from InSAR: a simulation study, *J. geophys. Res.,* **19**(B09406), 1–13.

Doin, M., Lasserre, C., Peltzer, G., Cavalié, O. & Doubre, C., 2009. Corrections of stratified tropospheric delays in SAR interferometry: validation with global atmospheric models, *J. app. Geophys.,* **19**(1), 35–50.

Funning, G.J., Parsons, B. & Wright, T.J., 2005. Surface displacements and source parameters of the 2003 Bam (Iran) earthquake from Envisat advanced synthetic aperture radar imagery, *J. geophys. Res.,* **19**(B09406), 1–23.

Ghiglia, D. & Romero, L., 1994. Robust two-dimensional weighted and unweighted phase unwrapping that uses fast transforms and iterative methods, *J. Optical Soc. Am. A,* **11**(1), 107–117.

Hooper, A., Segall, P. & Zebker, H., 2007. Persistent scatterer interferometric synthetic aperture radar for crustal deformation analysis with application to Volcan Alcedo, Galapogos, *J. geophys. Res.,* **112**(B07407), doi:10.1029/2006JB004763.

Hsu, Y., Bechor, N., Segall, P., Yu, S. & Kuo, L., 2002. Rapid afterslip following the 1999 Chi-Chi, Taiwan earthquake, *Geophys. Res. Lett.,* **29**(1754), doi:10.1029/2002GL014967.

Hsu, Y., Segall, P., Yu, S., Kuo, L. & Williams, C., 2007. Temporal and spatial variations of post-seismic deformation following the 1999 Chi-Chi, Taiwan, earthquake, *Geophys. J. Int.,* **169,** 367–379.

Jouanne, F. *et al.*, 2011. Post-seismic deformation in Pakistan after the October 8, 2005 earthquake: evidence of afterslip along a flat north of the Balakot-Bagh thrust, *J. geophys. Res.,* **116**(B07401), doi:10.1029/2010JB007903.

Kaneda, H. *et al.*, 2008. Surface rupture of the 2005 Kashmir, Pakistan, earthquake and its active tectonic implications, *Bull. seism. Soc. Am.,* **98**(2), 521–557.

Kumar, S., Wesnousky, S., Rockwell, T., Ragona, D., Thakur, V. & Seitz, G., 2001. Earthquake recurrence and rupture dynamics of Himalayan Frontal Thrust, India, *Science,* **19**(5550), 2328–2331.

Lavé, J., Yule, D., Sapkota, S., Basant, K., Madden, C., Attal, M. & Pandey, R., 2005. Evidence for a great medieval earthquake (approximate to 1100 ad) in the central Himalayas, Nepal, *Science,* **19**(5713), 1302–1305.

Leprince, S., Barbot, S., Ayoub, F. & Avouac, J., 2007. Automatic and precise orthorectification, coregistration, and subpixel correlation of satellite images, application to ground deformation measurements, *IEEE Trans. Geosci. Remote Sens.,* **45**(6), 1529–1558.

Michel, R., Avouac, J. & Taboury, J., 1999a. Measuring ground displacements from SAR amplitude images: application to the landers earthquake, *Geophys. Res. Lett.,* **19**(7), 875–878.

Michel, R., Avouac, J. & Taboury, J., 1999b. Measuring near field coseismic displacements from SAR images: application to the landers earthquake, *Geophys. Res. Lett.,* **19**(19), 3017–3020.

Okada, Y., 1985. Surface deformation due to shear and tensile faults in a half-space, *Bull. seism. Soc. Am.,* **75**(4), 1135–1154.

Parsons, T., Yeats, R., Yagi, Y. & Hussain, A., 2006. Static stress change from the 8 October, 2005 M = 7.6 Kashmir earthquake, *Geophys. Res. Lett.,* **33**(L06304), doi:10.1029/2005GL025429.

Pathier, E., Fielding, E.J., Wright, T.J., Walker, R., Parsons, B.E. & Hensley, S., 2006. Displacement field and slip distribution of the 2005 Kashmir earthquake from SAR imagery, *Geophys. Res. Lett.,* **19**(L20310), 1–5.

Perfettini, H. & Avouac, J., 2004. Postseismic relaxation driven by brittle creep: a possible mechanism to reconcile geodetic measurements and the decay rate of aftershocks, application to the Chi-Chi earthquake, Taiwan, *J. geophys. Res.,* **109**(B02304), doi:10.1029/2003JB002488.

Rosen, P., Hensley, S., Peltzer, G. & Simons, M., 2004. Updated repeat orbit interferometry package released, *Trans., Am. Geophys. Union,* **8**(5), 47.

Schmidt, D.A. & Bürgmann, R., 2003. Time-dependent land uplift and subsidence in the Santa Clara Valley, California, from a large interferometric synthetic aperture radar data set, *J. geophys. Res.,* **19**(B9), ETG4.1–ETG4.13.

Trouvé, E., Nicolas, J. & Maitre, H., 1998. Improving phase unwrapping techniques by the use of local frequency estimates, *IEEE Trans.Geosci. Remote Sens.,* **36**(6), 1963–1972.

Wang, H., Ge, L., Xu, C. & Du, Z., 2007. 3-D coseismic displacement field of the 2005 Kashmir earthquake inferred from satellite radar imagery, *Earth Planets Space,* **19**(5), 343–349.

Yan, Y., Trouvé, E., Pinel, V., Mauris, G., Pathier, E. & Galichet, S., 2012. Fusion of D-InSAR and sub-pixel image correlation measurements for coseismic displacement field estimation: application to the Kashmir earthquake (2005), *Int. J. Image Data Fusion,* **3**(1), 71–92.

Yu, S., Hsu, Y., Kuo, L. & Chen, H., 2003. GPS measurement of postseismic deformation following the 1999 Chi-Chi, Taiwan, earthquake, *J. geophys. Res.,* **108**(2520), doi:10.1029/2003JB002396.

Zebker, H., Rosen, P. & Hensley, S., 1997. Atmospheric effects in interferometric synthetic aperture radar surface deformation and topographic maps, *J. geophys. Res.,* **19**(7), 547–563.

SUPPORTING INFORMATION

Additional Supporting Information may be found in the online version of this article:

Figure S1. Phase delay/elevation ratio derived from (a) interferogram (b) meteorological model. Track 191 (2004/10/18–2005/11/07). In (a), each point represents an area ($\sim$1 $\times$ 1 km) selected in the far field where there is no deformation. In (b), the points correspond to elevation levels provided by the meteorological model.

Figure S2. Example of quadtree downsampling. Track 191 (2004/10/18–2005/11/07), D-InSAR measurement. Original size: 2564 $\times$ 1364 pixels. 2976 points are taken after the downsampling. The threshold of the displacement variance is 0.0003 m^2.

Figure S3. Profile (AB), averaged over a 151 pixels large band, used for comparisons between data observations and model predictions for décollement tests. The background image is the Up component of the 3-D surface displacement.

s2005Kashmirarche_1seg.slp. Text file of the one segment slip distribution model

s2005Kashmirarche_2seg.slp. Text file of the two segments slip distribution model (http://gji.oxfordjournals.org/lookup/supp1/doi:10.1093/gji/ggs102/-/DC1)

Please note: Oxford University Press is not responsible for the content or functionality of any supporting materials supplied by the authors. Any queries (other than missing material) should be directed to the corresponding author for the article.